Infrared detection of tungsten cracking on actively cooled ITER-like component during high power experiment in WEST

Q. Tichit, A. Durif, J. Gaspar, Y. Anquetin, Y. Corre, M. Diez, L. Dubus, M. Firdaouss, J. Gerardin, A. Grosjean, et al.

Nuclear Materials and Energy 37 (2023) 101537

Contents lists available at ScienceDirect

Nuclear Materials and Energy

journal homepage: www.elsevier.com/locate/nme

Infrared detection of tungsten cracking on actively cooled ITER-like component during high power experiment in WEST

Q. Tichit [a], A. Durif [a], J. Gaspar [b], Y. Anquetin [b], Y. Corre [a], M. Diez [a], L. Dubus [a], M. Firdaouss [a], J. Gerardin [a], A. Grosjean [c], J.P. Gunn [a], K. Krieger [d], M. Missirlian [a], S. Ratynskaia [e], P. Reilhac [a], M. Richou [a], F. Rigollet [b], the WEST team

[a] CEA, Institute for Research on Fusion by Magnetic confinement, 13108 St-Paul-Lez-Durance, France
[b] Aix Marseille Univ, CNRS, IUSTI, Marseille, France
[c] Department of Nuclear Engineering, University of Tennessee, Knoxville, TN 37996, USA
[d] Max-Planck-Institut für Plasmaphysik, 85748 Garching b, München, Germany
[e] Space and Plasma Physics - KTH Royal Institute of Technology, SE-10044, Stockholm, Sweden

ARTICLE INFO

Keywords:
Divertor
Plasma-facing components
Actively cooled
Tungsten cracking
High power
Ductile failure
Thermal cycling

ABSTRACT

The consequences of tungsten (W) damaging processes, such as cracking and melting, on divertor lifetime and plasma operation are high priority issues for ITER. A sustained melting experiment was conducted in WEST using a 2 mm deep groove geometry on the upstream mono-block (MB) to overexpose the sharp leading edge (LE) of the downstream MB. W-cracking has been evidenced for the first time with a very high spatial resolution infrared camera before tungsten melting was reached. These cracks develop when the monoblock temperature is about 2600 °C, thus higher than both ductile to brittle transition and softening threshold of tungsten, suggesting that these cracks are different from the ones observed in previous campaigns where brittle failure was involved, because of transient events on cold monoblock. Post-exposure analyses have been performed on the damaged monoblock, highlighting 12 main cracks on the LE, with a width varying from 33 μm to 77 μm, and an average spacing of 0.45 mm. Parallel heat flux about 90 MW/m^2 has been derived from infrared temperature measurements, with a heat flux decay length on the target of 4 mm. The T-REX modelling code suggest here that with these thermal inputs, a crack can initiates due to thermal cycling without disruption, with a ductile failure, under 1 to 5 cycles for a tungsten DBTT varying from 400 °C to 500 °C.

Introduction

Since the purpose of the divertor is to ensure continuous power exhaust in the tokamak devices, it is of prime interest to maintain its integrity and thus to well understand the mechanisms that leads to plasma facing components damaging. In WEST phase I, the lower divertor was equipped with a mix of W-coated graphite component and actively cooled ITER-like Plasma Facing Units (PFUs). The PFUs technology consists of tungsten monoblocks (MBs) bonded on a CuCrZr cooling tube, with ≈ 0.5 mm toroidal gaps between blocks [1]. Tungsten (W) monoblocks (MBs) cracking has already been observed at both leading and trailing edges of the MBs during previous WEST C1-C3 experimental campaigns [2]. At this time, the MB were unshaped and prone to intense heat load on the leading edge (in particular when two consecutive PFUs are misaligned). As the MB heat load derived from IR data [3] and embedded sensors [4] in C3 experimental campaign were small (below 3 MW.m^{-2} on the top surface) the thermal conditions did not allow tungsten softening and ductile cracking. Numerical simulations and post-exposure analysis suggested that the cracks highlighted during these experiments have been initiated during the cooling phase after transient events such as disruptions [2,5]. During this type of events the high heat flux deposited on a very short time leads to brittle failure of the MB when the stress exceeds the yield stress on cold component.

The melting experiment during the C5 campaign in WEST (2019–2020), were conducted with high injected power leading to higher heat flux (up to 6 MW/m^2) than measured during the C3 experimental campaign. One PFU was deliberately overexposed (2.3 mm height exposed area (Fig. 1)) to the very high parallel heat flux to reach tungsten melting, with a dedicated magnetic configuration and MB design (see section 2). Here, for the first time, cracks have been detected during operation, with the very high spatial resolution infra-red camera (VHR) of WEST, thanks to the cavity effect (further detailed in section 3). These cracks initiated when the surface temperature of the MB exceed both the ductile to brittle transition temperature (DBTT) and the softening threshold of the tungsten ($T_{W,rx}$) (Fig. 2) ($400^{\circ}C \leq DBTT_w \leq 500^{\circ}C$ [5,6],

https://doi.org/10.1016/j.nme.2023.101537
Received 2 August 2023; Received in revised form 2 October 2023; Accepted 11 October 2023
Available online 18 October 2023

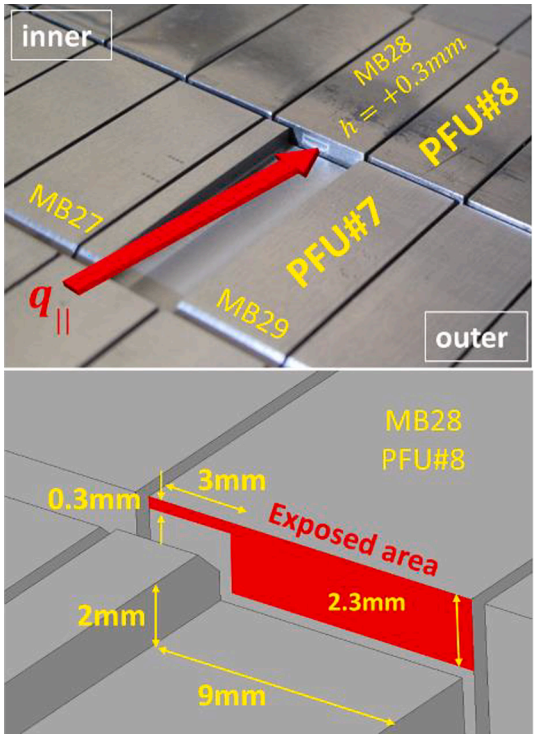

Fig. 1. Specific monoblock design manufactured for the melting experiment.

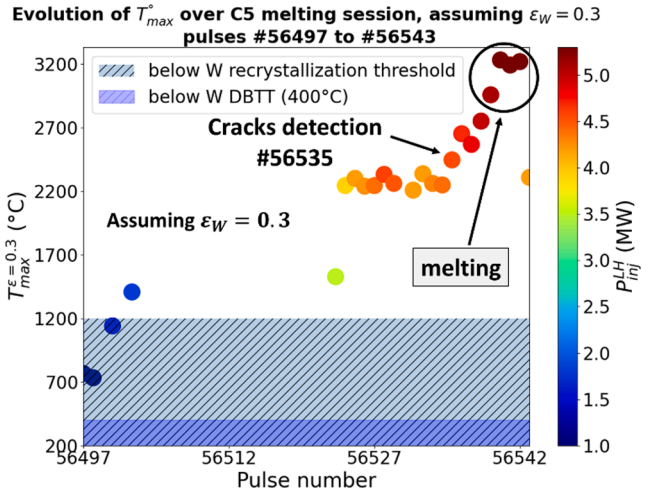

Fig. 2. Maximal temperature and injected LH power over the C5 melting session. Only pulses with duration over 3 s.

$T_{W,rx}$ 1200°C), as the maximal temperature on the component is about 2600 °C. These conditions suggest that these cracks probably initiate due to a different mechanism from the ones observed in the previous campaigns (brittle failure on cold component). The present work aims at verifying relying on the use of the T-REX tool [7], the viability of a ductile cracking before tungsten melting, in steady state operation phase due to heating/cooling cycling.

The section 2 presents the machine and plasma configuration, as well as the VHR camera. Section 3 focusses on the cracks detection and post-exposure characterization. The heat load is assessed and the T-REX tool are described in section 4. Finally the results from T-REX tool are presented in section 5.

Experimental set-up

Plasma facing unit design

For the C5 experimental campaign of WEST, two 30° sectors of the divertor were equipped with 38 ITER-like PFUs (plasma facing unit) [8]. Each of these sectors are made of 38 PFUs, and each of these PFUs consists of 35 tungsten MBs joined on a CuCrZr pipe. The following study focusses on MB28 PFU#8 located on the low field side (LFS) of the divertor and on the maximum heat flux area due to the ripple modulation of the magnetic field [9]. A dedicated design was manufactured for C5 melting experiment in order to maximize the power density applies on the MB28 PFU#8 [10]. PFU#8 have a flat top surface (i.e. without 1° bevel), with sharp leading edges (LE) and it is 0.3 mm vertically misaligned with respect to the previous PFU (PFU#7). Moreover, the upstream MB28 (PFU#7) was machined with a 9x2 mm (width × depth) groove on its surface. The poloidal LE of the MB28 PFU#8 is then overexposed on a 9 mm wide and 2.3 mm depth area (2 mm groove + 0.3 mm misalignment) [10](Fig. 1).

The very high spatial resolution IR camera

The spectral radiance of the MBs ($L_{IR,\lambda}(T_{MB})$) is monitored here with the WEST very high spatial resolution infrared camera (VHR). With a spatial resolution about 0.1 mm/px [11], this diagnostic is well adapted for studies at the MB scale. The VHR operates with a medium wavelength infrared (MWIR) filter centered on $\lambda = 3.9 \pm 0.1$ µm. The temperature threshold is about 250 °C (black body temperature).

The spectral radiance $L_{IR,\lambda}$ can be expressed by the following equation when the self-reflection of the tungsten component is neglected:

$$L_{IR,\lambda}(T_{MB}) = \varepsilon_{W,\lambda}(T_{MB})L_{BB,\lambda}(T_{MB}) + (1 - \varepsilon_{W,\lambda}(T_{wall}))L_{BB,\lambda}(T_{wall}) \quad (1)$$

where $L_{IR,\lambda}$ is the spectral radiance measured by the VHR at the wavelength λ, $L_{BB,\lambda}$ the black body spectral radiance, $\varepsilon_{W,\lambda}$ the tungsten emissivity, T_{MB} the MB temperature and T_{wall} the temperature of the vacuum vessel wall (it means the background).

As the temperature of the MB is high enough regarding the wall temperature (T_{MB} 10 × T_{wall}), the second term of the equation (1) becomes negligible, and the spectral radiance of the component $L_{IR,\lambda}(T_{MB})$ appears directly proportional through its emissivity, to its black body radiance at the same temperature.

As the IR data processing system consider $\varepsilon_{W,\lambda}$ equal to 1, the experimental temperature profiles obtained from the raw IR data are black body (BB) profiles (T^{BB}_{IR}). These black body profiles need to be converted into corrected profiles by using emissivity correction. Post-exposure measurements shown that on the strike point location (erosion area), the emissivity of the component is close to the value for the pristine tungsten ($\varepsilon_{W,\lambda} = 0.1$) [12]. The temperature dependency of the emissivity is studied in [13]. By linear extrapolation at 2600 °C, for this study, the BB profiles will be corrected by assuming $\varepsilon_{W,\lambda} = 0.3$. The resulting corrected temperature profiles will be called $T^{0.3}_{IR}$. Here, the viability of the linear extrapolation is justified by the quasi linear behavior of the emissivity variation in this temperature range (see Hagen-Rubens curve [14]).

Magnetic equilibrium and plasma exposure

A dedicated plasma scenario with a farther outer strike point (OSP) has been set-up to maximize the integrated power into the groove and reach tungsten melting on MB28 PFU#8. The X-point height varies from 102 to 112 mm. Plasma current is equal to 500kA with a magnetic field $B_T = 3.7$ T. The heating power is injected with the two lower hybrid (LH) launchers for 5 s [10].

C5 melting experiment extends over about 50 pulses from the pulse #56492 to the pulse #56543 for a total of 104 s of plasma exposure for

the MB28. This plasma time is computed by excluding all the pulses shorter than 3 s (21 pulses remain) and removing 3 s to all the other pulses in order to roughly keep only the diverted phase. The injected LH power (P_{inj}^{LH}) was increased gradually during the session to reach 5.5 MW over 5 s. Tungsten melting occurred during the four pulses with P_{inj}^{LH} between 5 and 5.5 MW over 5 s (pulses #56538 to 56542, circled in black in Fig. 2). Along the whole session, the maximal temperature (assuming $\varepsilon_{W,\lambda}$ 0.3 mm) is higher than $DBTT_w$ and for most of the pulses higher than $T_{W,rx}$ (Fig. 2).

In-operando cracks detection and post-operation characterization

For the first time, cracks are detected in operation on a component surface thanks to the VHR IR camera. Indeed, we can observe a local increase of the apparent temperature (around 10 to 20 °C) due to the multiple reflections which occur inside the cracks. This effect is known as the cavity effect. The cracks are visible on both VHR images (Fig. 3) and poloidal temperature profiles during the cooling phase (Fig. 4) after the pulse #56535. Cracks cannot be observed neither during the temperature rise phase, nor during the heating plateau. There is not enough signal before the power injection because the component is cooling down to $70^{\circ}C$ between each pulse thanks to the active cooling, and the slight temperature enhancement due to the cavity effect becomes undetectable at high temperatures, during the heating plateau. Indeed, the cavity effect is still present at high temperatures, so theoretically the cracks should detectable. However, the very strong temperature gradient in the poloidal direction –almost 200 °C per millimeter (Fig. 4)–, and the fact that the strike point moves slightly during the pulse enter in competitions with the cavity effect, and tend to blur is effect. Regarding Fig. 4, the cracks seems to initiate with an injected LH power $P_{inj}^{LH} \approx 4.6MW$ over 5 s, which corresponds to the pulse #56535. Here the temperature of the MB is about 2600 °C on the LE. Follow-up of the cracks has been performed with the VHR during progressive increase of LH power up to the melting point reach for the pulse #56541. In this temperature range (from crack initiation ≈ 2600 °C, up to melting point ≈ 3400 °C), tungsten softening due to restoration and recrystallization is expected.

The twelves main cracks on the LE will be named C_n with n from 1 to 12 from high field side (HFS) to low field side (LFS). Five main cracks are visible on both temperature profiles and IR images (C_1, C_3, C_5, C_6 and C_8). C_5 disappears from IR observations between pulse #56538 and #56541, which corresponds, to the pulses where tungsten melting occurred (Fig. 3 and Fig. 4). This is due to melt bridging the crack [15,16,17]. But it reopened later, as it is visible on post-exposure observations.

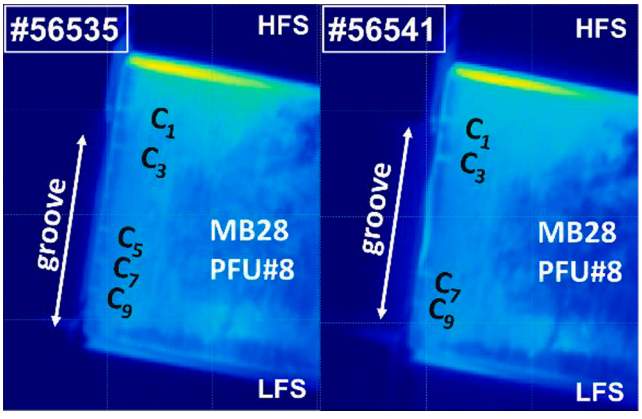

Fig. 3. View of MB28 PFU#8 with the VHR IR camera. Pulses #56538 (left) before melting and #56543 (right) after melting.

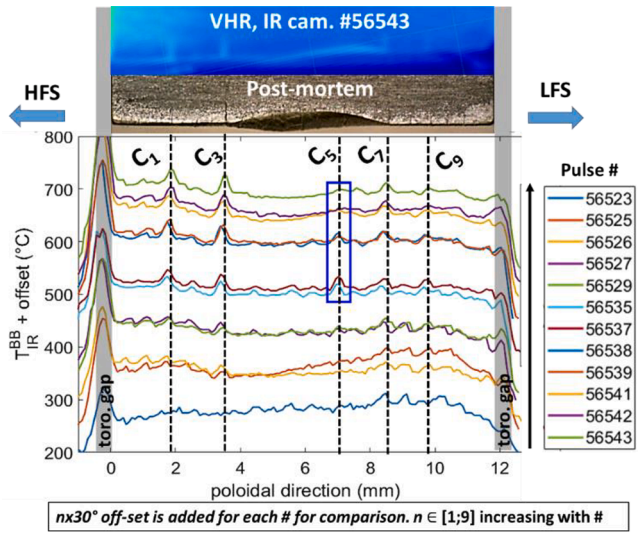

Fig. 4. Detection of cracks on IR poloidal temperature profiles (MB28 PFU#8) compared to post-exposure and VHR images.

The confocal microscopy observations performed after C5 campaign on MB28 PFU#8 highlights both vertical and horizontal cracking on the overexposed LE (Fig. 5 **c, d, e**). The main cracks vary in width from 26 µm (C_5) to 77 µm (C_3) and propagate on the top surface in the toroidal direction up to 2.5 mm. Crack number 3 (C_3) is the largest one observed post experiments (Fig. 5). The spacing between the cracks varies from 0.23 mm to 1.47 mm. The average spacing is 0.45 mm which is comparable to the value of the previous work [5], but with a higher standard deviation (0.27 mm). This is explainable by the molten area, where the cracks analysis is not relevant because of all the phenomenon occurs in this zone. We can note that the density of cracks seems to be higher on the LFS.

Methodology of crack mechanism identification

Heat load assessment

To explain the cracks appearance and the damage mechanisms

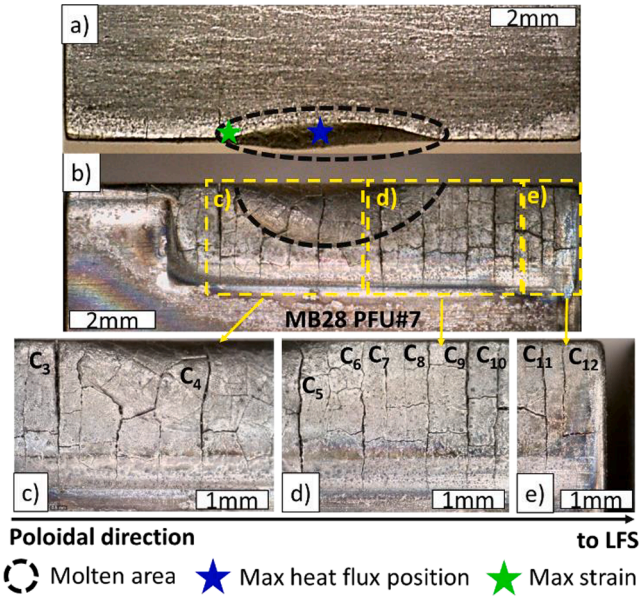

Fig. 5. Post-exposure observations on MB28 PFU#8. Top view a), LE on poloidal view b), zooms on LE c), d) and e).

occurred for the tungsten leading edge, the T-REX modelling are performed and relying on assumptions such as the relevant WEST heat load.

The heat load on the MB is derived from the comparison between the temperature profiles simulated with finite element method (FEM) and the experimental ones obtained via the VHR camera. Three-dimensional parametric heat load is generated based on optical approximation (OA). The optical approximations neglects the Larmor radius, assuming thus that all the particles follow strictly the magnetic field lines (MFL). Using the OA, the heat flux on the different surfaces of the MB can be computed as follow, depending on α the incident angle of the MFL and the parallel heat flux at the target location ($q_{\parallel}^{t}$):

$$q_n = q_{\parallel}^{t}\sin\alpha \tag{2.1}$$

$$q_{sh} = q_{\parallel}^{t}\sin(\alpha+\beta) \tag{2.2}$$

$$q_{toro} = q_{\parallel}^{t}\sin\theta\| \tag{2.3}$$

$q_{\parallel}^{t}$, q_n and q_{sh} are respectively the incident heat fluxes arriving on the divertor target, on the top surface (normal incidence) and on the sharp LE side. α is the incident grazing angle of the MFL, β the angle between the top surface and the side of the MB ($\beta = 90^{\circ}$ for sharp LE), and $\theta\|$ is the angle between the projection of the MFL on the top surface, and the toroidal surface.

$q_{\parallel}^{t}$ is computed by using the equation (3) [18]. The λ_q^t parameter is the decay length value at the target location. It describes the evolution of the heat flux in the Scrape-Off layer (SOL) part. S^t is the spreading factor of the Gaussian part, also at the target location. This parameter characterizes the heat flux diffusion in the private flux region (PFR).

$$q_{\parallel}^{t} = \frac{q_0}{2}\exp\left(\left(\frac{S^t}{2\lambda_q^t}\right)^2 - \frac{\bar{s}}{\lambda_q^t}\right) erfc\left(\frac{S^t}{2\lambda_q^t} - \frac{\bar{s}}{S^t}\right) + q_{BG} \tag{3}$$

where q_0 is the separatrix value, q_{BG} represent the background contribution. $\bar{s} = s - s_0$, where s and s_0 are respectively the relative position and the OSP position along poloidal axis.

Poloidal and toroidal temperature profiles are extracted from each simulation. These simulated temperature profiles will be named T_{FEM}. To simulate the pixel size, optical blurring and deformation, these numerical profiles are convoluted with the modulation transfer function (MTF) of the VHR camera to obtain synthetic temperatures (T_{MTF}) [19]. This MTF is modelled by a Gaussian function with an 0.175 mm standard deviation [20]. Since the temperature gradient is higher in the toroidal direction, the effect of the MTF will be more significant on toroidal profiles than on poloidal ones. As the temperature gradient is very high over the first millimeter of the toroidal profile, it is sufficient to take a poloidal profile 2 or 3 mm from the LE to make the effect of the MTF negligible. But as it is necessary here to access the maximum temperature, the profile must be taken on the LE. To represent properly the MTF effect on the maximum temperature, 25 toroidal profiles were extracted all along the MB. Then the MTF of the VHR camera is applied to each of them, and finally the poloidal profile is rebuilt from these synthetic toroidal profiles. *FEM* and *MTF* profiles are reported on Fig. 6 to be compared with the experimental *IR* profiles. Once the black body temperature profile is extracted on the LE from the VHR movie (black curve on Fig. 6), it is corrected by using the assumed emissivity $\varepsilon_{W,\lambda} = 0.3$ (see section 2.2). The $T_{IR}^{0.3}$ obtained represents an approximation of the true temperature on the MB surface (blue curve on Fig. 6). The maximum temperature is 6 mm far from the upper toroidal edge (LFS edge).

To match the VHR IR profiles, the simulation takes the following inputs: $\lambda_{q^-}^t = 4mm$, $S^t = 2mm$ and $q_{\parallel}^t = 90MW/m^2$ with a strike point 4 mm far from the upper toroidal edge. By assuming $2.5 < \alpha < 2.6°$, the heat flux on the top surface reach $q_n \approx 4$ MW/m^2 while q_{sh} is about 90 MW/m^2. Due to the magnitude 10 between the maximum heat flux on the toroidal gaps and the one on the top surface (magnitude 100 compared to the leading edge), these heat fluxes are neglected in this section and the T-REX tool is run with only heat flux on top and poloidal surfaces.

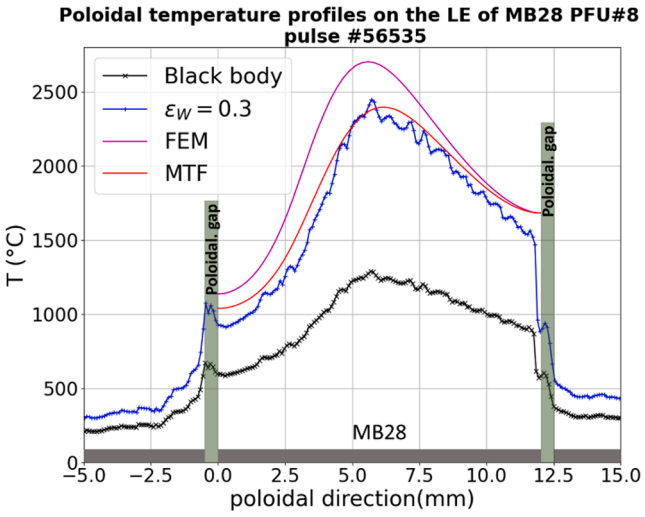

Fig. 6. Poloidal temperature profiles along the leading edge of MB28 PFU#8. T_{IR}^{BB} in black, $T_{IR}^{0.3}$ in blue, T_{FEM} in magenta (assuming $\lambda_q^t = 4$ mm and $S^t = 2$ mm) and T_{MTF} in red (poloidal profile rebuilt from 25 synthetic toroidal profiles). The three grey areas at the bottom represent MB27, 28 and 29 respectively. The green areas materialize the 0.5 mm poloidal gaps between the MBs. (For interpretation of the references to colour in this figure legend, the reader is referred to the web version of this article.)

The T-REX tool: Assumption and model

T-REX is a modelling code based on an elastic-viscoplastic model, which considers the progressive tungsten mechanical properties changes due to softening [7]. Outputs of the tool give the opportunity to study the evolution of the tungsten softening fraction as well as plastic strain accumulation over the thermal cycles to assess the component lifetime (number of cycles to failure). Here the simulations are run for 5 thermal cycles of 10 s (5 s ON/ 5 s OFF), which is consistent with both the duration of the power plateau, and the cooling time performed in WEST. The softening kinetics and the mechanical behavior taken into account in the model for tungsten are the same as presented in [7].

3D model considered here is presented figure Fig. 7. Monobocks model is composed of 55,896 linear elements. Routine developed at CEA [21] is used to calculate the heat transfer coefficients assuming the following WEST cooling conditions: T = 70 °C, v = 10 m/s and P = 3.3 MPa. Thermal heat flux assessed in the previous section is applied along the curvilinear abscissa (in blue Fig. 7) with the maximum peak heat flux is applied on the leading edge. The pattern of the heat flux along the curvilinear abscissa considered in the upcoming modelling is presented in Fig. 7 (bottom).

Numerical results and discussions

Simulation related to the pulse #56535

In the following a special focus is made on pulse #56535. For this specific pulse, the cracks have been detected via VHR camera for the first time (Fig. 4). 90 MW/m^2 peak heat flux assessed in the previous section is consider at the LE in the upcoming T-REX modelling.

Fig. 8.b presents the softening gradient obtained in the tungsten bloc after five thermal cycles. In the poloidal gap, the model predicts 90 to 100 % softening over the first 2.3 mm and softening gradient between 2.3 and 3.4 mm. Likewise on the top surface, with almost 100 % softening on the first 1.6 mm and softening gradient until 2.7 mm (Fig. 8.**b**).

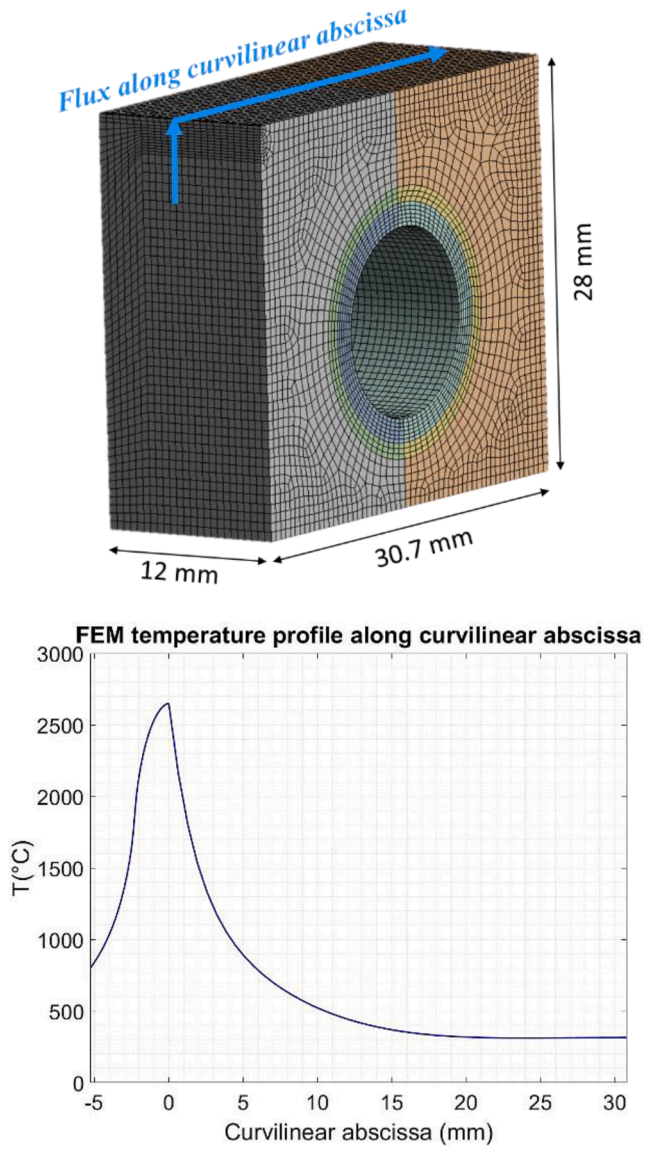

Fig. 7. Numerical model assumed (top) and temperature profile along the curvilinear abscissa (bottom).

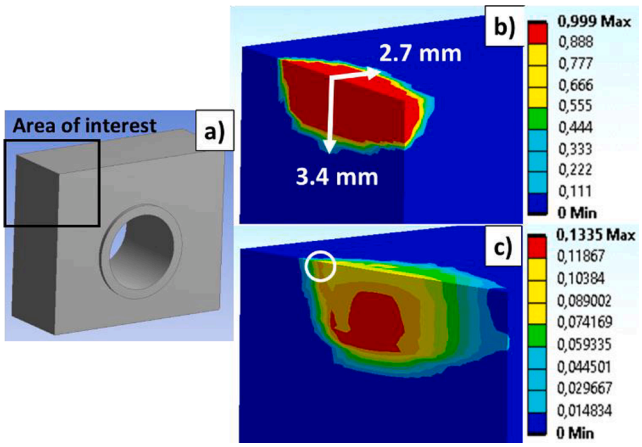

Fig. 8. Results from T-REX code. a) View of a MB with sharp LE and flat top surface. b) Tungsten softening map. c) Plastic strain accumulation map. In red the maximum value. (For interpretation of the references to colour in this figure legend, the reader is referred to the web version of this article.)

As shown in Fig. 8.**c**, the maximum plastic strain rate is located at the bottom of the overexposed area (2.1 mm below the LE). The lifetime assessment given is based on the plastic strain increment generated over a thermal cycle which is decomposed as two quantities: one related to a fraction of plastic increment generated at high temperature (above the tungsten DBTT) and one related to a fraction of plastic increment estimated at lower temperature (below the tungsten DBTT). The method used to assess the lifetime is presented in [22]. A minimum lifetime was founded below the LE where the maximum plastic strain is assessed (1.2 cycles) compared to the maximum strain at the LE (4.8 cycles) assuming 350 °C. Nevertheless, regarding the LE damaged observed the upcoming work is build based on the maximum of plastic strain extracted at the LE. The lifetime is therefore calculated using the maximum value of plastic strain accumulation at the LE. This maximum value is located at about 3.5 mm from upper toroidal edge for $q_{\parallel}^{t} = 90$ MW/m^2, which corresponds to the approximate location of the largest crack (C_3, at 3.6 mm, Fig. 5). Assuming conservative DBTT (350 °C) modelling assessed that crack should occur at the LE after 4.8 cycles (Table 1).

Discussions

During the session, two disruptions occurred respectively at the end of pulses #56529 and #56530. These events happened when the LH power was decreasing. Their related impact remains to be precisely assessed. Nevertheless, no disruption occurred between pulses #56531 and #56535, i.e. five pulses including #56535, which may be sufficient to initiates cracks with $q_{\parallel}^{t} = 90$ MW/m^2. As the most impacting parameters for the lifetime assessment are the peak parallel heat flux intensity ($q_{\parallel}^{t}$) and the tungsten DBTT, simulations have been run assuming different values of $DBTT_W$ (from 350 °C to 500 °C) and $q_{\parallel}^{t}$ (from 80 to 90 MW/m^2) The results are presented on the Table 1.

With the heat load derived from the IR temperature measurement for the pulse #56535 ($q_{\parallel}^{t} = 90 MW/m^2$), the simulation predicts 1.1 to 2.8 cycles to crack, depending on the $DBTT_W$ value. This number increases to reach 4.8 cycles if $DBTT_W$ decreases to 350 °C (Table 1). By looking at the pulse history before the pulse #56535, we can note than the 9 previous pulses are quite similar in terms of injected power and maximal IR black body temperature. Indeed, the maximal deviation for the temperature stayed under 7 % as it is summed up in the Table 2. As the evolution of the maximal temperature with the parallel heat flux is quasi linear, we can suppose a maximal error of 10 % on the heat flux estimation for these 9 pulses. It is thus reasonable to assume that the parallel heat flux for this 9 pulses is between 80 and 90 MW/m^2 based on the estimation for the pulse #56535. With $q_{\parallel}^{t} = 80$ MW/m^2 and $DBTT_W = 350$ °C, T-REX predict 11.7 cycles to failure.

In this condition there are enough pulses (cycles heating/cooling) before the #56535 to explain the initiation of at least one of the cracks (C_3, the largest one) even for DBTT value lower than the one expected for the component (case at $DBTT_W = 350$°C) with $q_{\parallel}^{t} = 90$ MW/m^2.

Conclusion

For the first time, progressive cracking of a monoblock leading edge is highlighted in operando in WEST tokamak. Based on the thermal in-

Table 1
Estimated lifetime of a tungsten bulk MB in number of cycle before crack initiation, in function of the $DBTT_W$ and $q_{\parallel}^{t}$.

Lifetime (number of cycles to crack)		
$DBTT_W$(°C)	$q_{\parallel}^{t} = 90$ MW/m^2	$q_{\parallel}^{t} = 80$ MW/m^2
350	4.8	11.7
400	2.8	–
500	1.1	–

Table 2
Pulse history before the #56535. Pulses corresponding to the minimal and maximal deviation are highlighted in bold. #56535 used as reference.

Pulse n°	$P_{inj}^{LH}(MW)$	$T_{IR,max}^{BB}(°C)$	$\Delta T_{max}(\%)$
56,525	4.3/5s	1230	−4.6
56,526	**4.4/4s**	**1205**	**−6.5**
56,527	4.4/5s	1207	−6.4
56,528	4.6/5s	1243	−3.6
56,529	**4.5/3.5 s**	**1252**	**−2.9**
56,531	4.3/5s	1235	−4.2
56,532	4.2/5s	1245	−3.4
56,533	4.3/5s	1214	−5.8
56,534	4.4/5s	1233	−4.3
56,535	4.6/5s	1289	0.0

puts derived from IR temperature measurements on the pulse #56535, the T-REX tool predicts a maximum of 11 thermal cycles before crack initiation at the leading edge. As there are 9 pulses before the #56535 with $q_{\parallel}^{t} \geq 80$ MW/m^2, this study shows that T-REX lifetime assessment are consistent with the WEST experiment number of cycles performed.

This study suggests thus a possible ductile cracking mechanism for at least the largest crack observed on the leading edge (C_3); but it remains to estimate a number of cycles to failure for each of the 12 main cracks, as there is a strain and stress gradient all along the LE of the tungsten MB. Moreover, for further investigation, and modelling, the $DBTT_W$ should be precisely study for the tungsten grade embedded in the WEST divertor.

CRediT authorship contribution statement

Quentin Tichit: Conceptualization, Investigation, Methodology, Formal analysis, Data curation, Writing – original draft. **A. Durif:** Software, Investigation, Formal analysis, Methodology, Writing – review & editing. **J. Gaspar:** Formal analysis, Investigation, Methodology, Writing – review & editing. **Y. Anquetin:** Formal analysis, Investigation. **Y. Corre:** Supervision, Formal analysis, Methodology, Investigation, Writing – review & editing. **M. Diez:** Formal analysis, investigation. **L. Dubus:** Software, Resources. **M. Firdaouss:** Formal analysis, Investigation, Software. **J. Gerardin:** Formal analysis, Investigation, Software. **A. Grosjean:** Formal analysis, Investigation, Methodology. **J.P. Gunn:** Investigation. **K. Krieger:** Investigation. **M. Missirlian:** Investigation. **S. Ratynskaia:** Software, Investigation. **P. Reilhac:** Investigation. **M. Richou:** Investigation. **F. Rigollet:** Investigation.

Declaration of Competing Interest

The authors declare the following financial interests/personal relationships which may be considered as potential competing interests: [Quentin TICHIT reports financial support was provided by European Consortium for the Development of Fusion Energy].

Data availability

Data will be made available on request.

Acknowledgements

“This work has been carried out within the framework of the EUROfusion Consortium, funded by the European Union via the Euratom Research and Training Programme (Grant Agreement No 101052200 — EUROfusion). Views and opinions expressed are however those of the author(s) only and do not necessarily reflect those of the European Union or the European Commission. Neither the European Union nor the European Commission can be held responsible for them.”

References

[1] M. Missirlian, J. Bucalossi, Y. Corre, F. Ferlay, M. Firdaouss, P. Garin, A. Grosman, D. Guilhem, J. Gunn, P. Languille, M. Lipa, M. Richou, E. Tsitrone, The WEST project: Current status of the ITER-like tungsten divertor, Fusion Eng. Des. 89 (7-8) (2014) 1048–1053, https://doi.org/10.1016/j.fusengdes.2014.01.050.
[2] M. Diez, Y. Corre, E. Delmas, N. Fedorczak, M. Firdaouss, A. Grosjean, J.P. Gunn, T. Loarer, M. Missirlian, M. Richou, E. Tsitrone, T. WEST Team, In situ observation of tungsten plasma-facing components after the first phase of operation of the WEST tokamak, Nucl. Fusion 61 (10) (2021) 106011, https://doi.org/10.1088/1741-4326/ac1dc6.
[3] N. Fedorczak, J. Gaspar, Y. Corre, A. Grosjean, X. Courtois, J.P. Gunn, R. Mitteau, R. Dejarnac, J. Bucalossi, E. Tsitrone, T. Loarer, S. Brezinsek, Cross diagnostics measurements of heat load profiles on the lower tungsten divertor of WEST in L-mode experiments, Nuclear Materials and Energy 27 (2021) 100961, https://doi.org/10.1016/j.nme.2021.100961.
[4] J. Gaspar, Y. Corre, N. Fedorczak, J.P. Gunn, C. Bourdelle, S. Brezinsek, J. Bucalossi, N. Chanet, R. Dejarnac, M. Firdaouss, J.-L. Gardarein, G. Laffont, T. Loarer, C. Pocheau, E. Tsitrone, the WEST Team, Divertor power loads and scrape off layer width in the large aspect ratio full tungsten tokamak WEST, Nucl. Fusion 61 (9) (2021) 096027, https://doi.org/10.1088/1741-4326/ac1803.
[5] A. Durif, M. Richou, J.-M. Bergheau, Y. Corre, M. Diez, P. Reilhac, J.P. Gunn, E. Tsitrone, Edge cracking of WEST tungsten actively cooled plasma facing components after plasma operation, Fusion Eng. Des. 188 (2023) 113441, https://doi.org/10.1016/j.fusengdes.2023.113441.
[6] V. Shah, J.A.W. van Dommelen, E. Altstadt, A. Das, M.G.D. Geers, Brittle-ductile transition temperature of recrystallized tungsten following exposure to fusion relevant cyclic high heat load, J. Nucl. Mater. 541 (2020) 152416, https://doi.org/10.1016/j.jnucmat.2020.152416.
[7] A. Durif, M. Richou, J.-.-M. Bergheau, L. Gallais, G. Kermouche, G. Pintsuk, T-REX: Numerical tool for tungsten damage assessment for DEMO, J. Nucl. Mater. 569 (153906569) (2022), https://doi.org/10.1016/j.jnucmat.2022.153906.
[8] J. Bucalossi *et al.*, « Operating a full tungsten actively cooled tokamak: overview of WEST first phase operation. », vol. 62, n° 04, 2022, doi: https://doi.org/10.1088/1741-4326/ac2525.
[9] C. Bourdelle, J.F. Artaud, V. Basiuk, M. Bécoulet, S. Brémond, J. Bucalossi, H. Bufferand, G. Ciraolo, L. Colas, Y. Corre, X. Courtois, J. Decker, L. Delpech, P. Devynck, G. Dif-Pradalier, R.P. Doerner, D. Douai, R. Dumont, A. Ekedahl, N. Fedorczak, C. Fenzi, M. Firdaouss, J. Garcia, P. Ghendrih, C. Gil, G. Giruzzi, M. Goniche, C. Grisolia, A. Grosman, D. Guilhem, R. Guirlet, J. Gunn, P. Hennequin, J. Hillairet, T. Hoang, F. Imbeaux, I. Ivanova-Stanik, E. Joffrin, A. Kallenbach, J. Linke, T. Loarer, P. Lotte, P. Maget, Y. Marandet, M.L. Mayoral, O. Meyer, M. Missirlian, P. Mollard, P. Monier-Garbet, P. Moreau, E. Nardon, B. Pégourié, Y. Peysson, R. Sabot, F. Saint-Laurent, M. Schneider, J.M. Travère, E. Tsitrone, S. Vartanian, L. Vermare, M. Yoshida, R. Zagorski, WEST physics basis, Nucl. Fusion 55 (6) (2015) 063017, https://doi.org/10.1088/0029-5515/55/6/063017.
[10] Y. Corre, A. Grosjean, J.P. Gunn, K. Krieger, S. Ratynskaia, O. Skalli-Fettachi, C. Bourdelle, S. Brezinsek, V. Bruno, N. Chanet, J. Coenen, X. Courtois, R. Dejarnac, E. Delmas, L. Delpech, C. Desgranges, M. Diez, L. Dubus, A. Durif, A. Ekedahl, N. Fedorczak, M. Firdaouss, J.-L. Gardarein, J. Gaspar, J. Gerardin, C. Guillemaut, M. Houry, T. Loarer, P. Maget, P. Mandelbaum, R. Mitteau, M. Missirlian, P. Moreau, R. Nouailletas, E. Nardon, C. Pocheau, A. Podolnik, P. Reilhac, X. Regal-Mezin, C. Reux, M. Richou, F. Rigollet, J.-L. Schwob, E. Thorén, P. Tolias, E. Tsitrone, Sustained W-melting experiments on actively cooled ITER-like plasma facing unit in WEST, Phys. Scr. 96 (12) (2021) 124057, https://doi.org/10.1088/1402-4896/ac326a.
[11] M. Houry, C. Pocheau, M.-H. Aumeunier, C. Balorin, K. Blanckaert, Y. Corre, X. Courtois, F. Ferlay, J. Gaspar, S. Gazzotti, A. Grosjean, T.h. Loarer, H. Roche, A. Saille, S. Vives, The very high spatial resolution infrared thermography on ITER-like tungsten monoblocks in WEST Tokamak, Fusion Eng. Des. 146 (2019) 1104–1107, https://doi.org/10.1016/j.fusengdes.2019.02.017.
[12] J. Gaspar, Y. Corre, F. Rigollet, M.-H. Aumeunier, E. Bernard, S. Brezinsek, X. Courtois, R. Dejarnac, M. Diez, L. Dubus, N. Ehret, N. Fedorczak, M. Firdaouss, M. Houry, M. Le Bohec, T. Loarer, C. Martin, V. Moncada, P. Moreau, C. Pocheau, P. Reilhac, E. Tsitrone, T. WEST Team, Overview of the emissivity measurements performed in WEST: in situ and post-mortem observations, Nucl. Fusion 62 (9) (2022) 096023, https://doi.org/10.1088/1741-4326/ac6f68.
[13] J. Gaspar, C. Pocheau, Y. Corre, N. Ehret, D. Guilhem, M. Houry, T. Loarer, T. h. Loewenhoff, C. Martin, C. Pardanaud, G. Pintsuk, M. Richou, F. Rigollet, H. Roche, G. Sepulcre, M. Wirtz, Emissivity measurement of tungsten plasma facing components of the WEST tokamak, Fusion Eng. Des. 149 (2019) 111328, https://doi.org/10.1016/j.fusengdes.2019.111328.
[14] M.A. Bramson (Ed.), Infrared Radiation, Springer US, Boston, MA, 1968.
[15] I. Jepu, G.F. Matthews, A. Widdowson, M. Rubel, E. Fortuna-Zaleśna, J. Zdunek, P. Petersson, V. Thompson, P. Dinca, C. Porosnicu, P. Coad, K. Heinola, N. Catarino, O.G. Pompilian, C.P. Lungu, Beryllium melting and erosion on the upper dump plates in JET during three ITER-like wall campaigns, Nucl. Fusion 59 (8) (2019) 086009, https://doi.org/10.1088/1741-4326/ab2076.
[16] L. Vignitchouk, S. Ratynskaia, R.A. Pitts, M. Lehnen, Simulations of liquid metal flows over plasma-facing component edges and application to beryllium melt events in JET, Nucl. Fusion 62 (3) (2022) 036016, https://doi.org/10.1088/1741-4326/ac47b7.
[17] S. Ratynskaia, K. Paschalidis, P. Tolias, K. Krieger, Y. Corre, M. Balden, M. Faitsch, A. Grosjean, Q. Tichit, R.A. Pitts, Experiments and modelling on ASDEX Upgrade and WEST in support of tool development for tokamak reactor armour melting

assessments, Nuclear Materials and Energy 33 (2022) 101303, https://doi.org/10.1016/j.nme.2022.101303.

[18] T. Eich, B. Sieglin, A. Scarabosio, W. Fundamenski, R.J. Goldston, A. Herrmann, Inter-ELM power decay length for JET and ASDEX Upgrade: Measurement and comparison with heuristic drift-based model, Phys. Rev. Lett. 107 (21) (2011), https://doi.org/10.1103/PhysRevLett.107.215001.

[19] Y. Corre, J.-L. Gardarein, R. Dejarnac, J. Gaspar, J.P. Gunn, M.-H. Aumeunier, X. Courtois, M. Missirlian, F. Rigollet, Methodology for heat flux investigation on leading edges using infrared thermography, Nucl. Fusion 57 (1) (2017) 016009, https://doi.org/10.1088/0029-5515/57/1/016009.

[20] A. Grosjean, M.H. Aumeunier, Y. Corre, M. Firdaouss, J. Gaspar, J. Gerardin, J. P. Gunn, X. Courtois, R. Dejarnac, M. Diez, L. Dubus, M. Houry, C. Pocheau, E. Tsitrone, Interpretation of temperature distribution observed on W-ITER-like PFUs in WEST monitored with a very-high-resolution IR system, Fusion Eng. Des. 168 (2021) 112387, https://doi.org/10.1016/j.fusengdes.2021.112387.

[21] J. Schlosser, J. Boscary, Finite elements calculations for plasma facing components, proceedings of specialist workshop on high heat flux component cooling, Grenoble (1993).

[22] A. Durif, M. Richou, G. Kermouche, J.-.M. Bergheau, Numerical study of the influence of tungsten recrystallization on the divertor component lifetime, Int J Fract 230 (2021) 83–98, https://doi.org/10.1007/s10704-021-00568-1.